Characterization of Flow Dynamics and Reduced-Order Description of Experimental Two-Phase Pipe Flow

Bianca Viggiano[a,*], Olaf Skjæraasen[b], Heiner Schümann[c], Murat Tutkun[d,e], Raúl Bayoán Cal[a]

[a]*Department of Mechanical and Materials Engineering, Portland State University, Portland, OR, USA*
[b]*Institute for Energy Technology, Department of Process and Fluid Flow Technology, Kjeller, Norway*
[c]*Sintef Petroleum AS, Trondheim, Norway*
[d]*Institute for Energy Technology, Department of Wind Energy, Kjeller, Norway*
[e]*Univeristy of Olso, Department of Mathematics, Blindern Oslo, Norway*

Abstract

Two-phase dispersed and slug flows in a pipe are investigated using proper orthogonal decomposition (POD). The data are acquired through tomographic reconstruction of X-ray measurements, where holdup, cross-sectional phase distributions and phase interface characteristics are obtained. Instantaneous phase fractions of the flow fields are analyzed and reduced order descriptions of the flow are achieved. The dispersed flow displays coherent features for the first few modes near the center of the pipe, representing the liquid-liquid interface location while the slug flow case shows coherent features that correspond to the cyclical formation of the slug in the first ten modes. For slug flow, the first two modes capture the liquid-dominated slug body region and the Taylor bubble/liquid film region, respectively. The reconstructions of the fields indicate that main features are observed in the low order descriptions utilizing less than one per cent of the degrees of freedom of the full order description. POD temporal coefficients a_1, a_2 and a_3 show interdependence for the slug flow case. The coefficients also describe the phase fraction holdup as a function of time for both dispersed and slug flow.

Keywords: Slug flow, dispersed flow, two-phase flow, multiphase flow, X-ray computed tomography, Proper orthogonal decomposition, Reduced order description

1. Introduction

Dispersed and slug flows appear in numerous industrial and environmental applications including petroleum production and transportation systems, bubble column reactors, boiler and heat exchanger tubes (Lindken & Merzkirch, 2002; Carneiro *et al.*, 2011; Balachandar & Eaton, 2010). These flow regimes are highly complex, containing pressure and density

*I am corresponding author
Email address: viggiano@pdx.edu (Bianca Viggiano)

gradients at the interface. The complexity of multiphase flows render many experimental measurement methods to be unusable and hinder numerical simulation accuracy (Hu *et al.*, 2014).

Dispersed flow, often turbulent, is characterized by the distribution of one fluid, the dispersed phase, within another fluid, the continuous carrier phase. Phase inversion is the phenomenon where the dispersed phase and the carrier phase spontaneously invert due to a small change in the operational conditions. Brauner & Ullmann (2002) developed a model to predict this phenomenon in a two-phase pipe flow system. The model is found to be useful, in particular, on critical water holdup values leading to phase inversion.

Although interface development is considered of secondary importance to the droplet size distribution in most studies on dispersed flows, droplet break-up and coalescence processes are correlated with the geometric characteristics of the interface (Balachandar & Eaton, 2010). In addition to experimental campaigns to perform detailed measurements, numerical simulations are also employed to analyze and characterize dispersed flows due to advancements in both computing power and storage availability. The complexity and scale of the dispersed fluid, however, deem these simulations either not accurate enough at the macroscale level or computationally expensive at the fully resolved scale (Balachandar & Eaton, 2010).

Industrially, one of the most interesting flow problems is considered to be slug flow, often occurring in transportation pipelines, networks and grids. Depending on the slug initiation mechanism, slug flows are divided into two groups. The first is terrain slugging which is an unsteady phenomenon and caused by the terrain effects in combination with liquid accumulation, gas blocking, pressure build-up, blow-out and suction. It is therefore dominated by kinematic effects coupled to the compressibility of the gas. The second group is called hydrodynamic slugging, the case studied in the paper. It appears due to unstable hydrodynamic interactions between the fluid phases and can achieve statistical stationarity. Contrary to the terrain slugging, the gas phase in hydrodynamic slugging is incompressible and the flow is dominated by the dynamic effects. Hydrodynamic slugging is intermittent and originates from stratified two- or three-phase flow where small perturbations create interface waves to grow via Kelvin-Helmholtz instabilities causing one phase to entirely occupy the cross-sectional area (Taitel & Dukler, 1976). Other causes of slug flow include wave coalescence at high flow rates and ramp-up of production or flow rates (Al-Safran *et al.*, 2005; Woods *et al.*, 2006).

Characterization of the slug flow is often carried out via determination of slug length and frequency, gas and liquid holdups and more recently turbulent velocity fluctuations and entrainment processes. From an operational perspective, tracking and predicting slug formation are crucial for steady processes and production. This is because most flow and processes simulators have models for slugging. Understanding the formation and development of slugs is therefore critical in mitigating the intermittent loading it inflicts on pipeline infrastructure over the life time of pipeline operation. Serious problems can occur as a result of pipe wall damages, especially in hydrocarbon production and transportation lines, leading to severe safety risks (Kvernvold *et al.*, 1984). In order to tune the system, and optimize the processes and production, one has to have information about slug characteristics because it

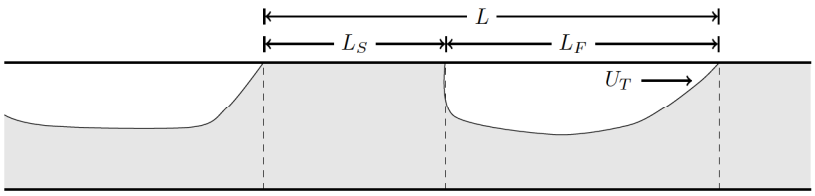

Figure 1: Diagram of slug unit with a length of L in the pipe.

can easily overload the processing equipment waiting in the end of the pipeline and causing an unwanted slow down, or perhaps unexpected halt in production.

The slug flow is depicted in figure 1. The elongated gas bubbles are shown in white and form along the top of the pipe and its translational velocity is denoted by U_T, which is also the translational velocity of a slug unit propagating along the pipe. The schematic includes the length of the liquid slug, L_S, the length of the slug unit, L, and the length of the film (or elongated bubble), L_F.

The slug (body) duration can be defined as the time interval between the passage of two successive slug body fronts (or Taylor bubble fronts) at a particular position and is determined by the gas volume fraction reaching a critical value at the top of the pipe. Given the translation velocity of elongated bubble (or the slug unit), U_T, time for passage of a slug unit is

$$\Delta t = L/U_T. \tag{1}$$

The slug frequency is determined by the number of slugs that pass through an area of interest during a controlled time interval. The average slug frequency is defined as

$$\langle f_s \rangle = \frac{1}{M-1} \sum_{k=1}^{M-1} \frac{1}{\Delta t}, \tag{2}$$

where M is the total number of slugs recorded and $\langle \cdot \rangle$ indicates time-averaging. **In what is often called fully developed slug flow, the statistical time and length scales for the slugs does not change with position along the pipe. Individual slugs, of course, differ from each other. Slug stability in this sense has been subject in many studies in literature. As detailed in Cook & Behnia (2000), minimum stable slug length is found to be approximately 10 pipe diameters in near horizontal conditions. The study indicated that the development length for stable slugs is close to 500-600 pipe diameters while average slug length is about 15 pipe diameters.**

Numerical and experimental studies have been performed to improve our understanding on slug flows and develop predictive models in particular for the length and shape distribution within the flow field (Carneiro *et al.*, 2011; Taitel & Dukler, 1976; Cook & Behnia, 2000). The two-fluid model, used frequently in numerical analysis, is formulated by considering the cross-sectional averaged governing equations of mass and momentum for each phase. Issa & Kempf (2003) took a mechanistic approach to the prediction of slug development, based on

the numerical solution of the one-dimensional transient two-fluid model equations. This approach minimized the need for phenomenological models which are significantly sensitive to change in boundary and initial conditions. Given the simplicity of the model, the results of the computations for slug characteristics and data obtained from literature have remarkable agreement.

Carneiro *et al.* (2011) examined slug flow both numerically and experimentally. The slug flow was simulated using the two-fluid model and the results were verified via experimental measurements. The two-fluid model was successful to predict frequency, velocity and slug length with differences varying from 10% to 20% for frequency and slug length compared to the experimental data.

In this study, the applicability of the proper orthogonal decomposition (POD) technique to multiphase flow is investigated. The POD has been used extensively in turbulence and other areas of mechanics ranging from structural vibration to fluid structure interaction. The application of proper orthogonal decomposition on the complex multiphase flow can be used to characterize the flow according to its modal components. Cizmas *et al.* (2003) studied the interactions of gas and solid phases in fluidized beds numerically to explore the implementation of a reduced order model via Galerkin methods. The data were obtained by simulating the two-dimensional uniform-minimal fluidization flow field. Phase space projections of the first three coefficients illustrated the presence of a low dimensional attractor. They found that the most dominant characteristics of the motion can be captured by a small number of POD modes.

In another study, Brenner *et al.* (2012) presented the derivation and implementation of a reduced-order model (ROM) based on proper orthogonal decomposition for non-isothermal multiphase flow. The ROM results were in agreement with the full order model at reference conditions. They generated a number of snapshot databases for both isothermal and non-isothermal flow to investigate effects of sampling rate for the test case. They found that as additional snapshots were added, error decreased as expected.

The POD examples discussed in the previous paragraphs use data produced by numerical simulations due to lack of experimental data needed to construct the kernel of POD integral equation, which is Fredholm integral equation of the second kind. In this paper, the POD analysis is performed on the flow using measurement data and focus mainly on two flow regimes, dispersed and slug flow, in a pipe. The instantaneous local phase fraction across the pipe cross-section is the main parameter to construct the kernel of proper orthogonal decomposition in this case.

The mathematical framework and application of the theory on multiphase flow is discussed in §2, and a brief description of the experimental setup is provided in §3. Results and discussion are presented in §4 and our conclusion follows in §5.

2. Theory

To gain further understanding of interface features and in turn characterize the mechanics of slug evolution, proper orthogonal decomposition is implemented. The POD was introduced to fluid mechanics as a decomposition technique to analyze turbulent velocity

signals (Lumley, 1967). The method of snapshots was developed by Sirovich (1987) and utilized when the flow measurements contain high spatial resolution in comparison to temporal resolution (cf. Holmes *et al.* (1998)).

The state variable is the instantaneous local phase fraction (volume fraction), $\phi(\mathbf{x}, t)$, to be used in the kernel for the decomposition. The instantaneous phase fraction describes the amount of a specified phase at a given location and time from 0 to 1, where 0 and 1 equate to non existence and only existing phase, respectively. In the following theoretical development, bold math symbols represent vectorial quantities.

The POD organizes the flow in an orthonormal basis of functions solution of the Fredholm integral equation:

$$\int_{\Omega} \mathbf{R}(\mathbf{x}, \mathbf{x}') \mathbf{\Psi}^{(p)}(\mathbf{x}') \mathrm{d}\mathbf{x}' = \lambda^{(p)} \mathbf{\Psi}^{(p)}(\mathbf{x}), \qquad p = 1, 2, \ldots \tag{3}$$

where Ω is the spatial domain considered, $\mathbf{\Psi}(\mathbf{x})$ is the set of basis functions and the eigenvalues are represented by λ. The term p represents the denumerable mode numbers in a bounded domain, and is limited by the number of grid points across the pipe cross-section, in this study given the quantity of interest is a scalar. The kernel of the POD, $\mathbf{R}(\mathbf{x}, \mathbf{x}')$, is the spatial correlation tensor and is defined as

$$\mathbf{R}(\mathbf{x}, \mathbf{x}') = \frac{1}{N} \sum_{n=1}^{N} \boldsymbol{\phi}(\mathbf{x}, t^n) \boldsymbol{\phi}(\mathbf{x}', t^n), \tag{4}$$

where the matrix $\boldsymbol{\phi}(\mathbf{x}, t^n)$ is the discretized phase fraction field. On index form, it can be written as $\phi_{ij}^n \equiv \phi(x_i, y_j, t^n)$, where x_i, y_j, t^n represent the discretized x-, y- and time-axes, respectively. Below, t^n is the time for sample n, and N refers to the total number of snapshots. The prime represents the spatial coordinate of another point in the domain. The kernel, $\mathbf{R}(\mathbf{x}, \mathbf{x}')$, is discrete (with four indices if $\mathbf{x}$ and $\mathbf{x}'$ are discretized coordinates in a 2D pipe cross section). Introducing an unknown coefficient vector $\mathbf{A}$, the deterministic field can be assumed to be:

$$\mathbf{\Psi}(\mathbf{x}) = \sum_{n=1}^{N} A(t^n) \boldsymbol{\phi}(\mathbf{x}, t^n), \tag{5}$$

which has the largest projection on the stochastic phase fraction field in a mean square sense. Through substitution of equations 4 and 5 into equation 3 and discretization, the integral equation can be expressed as an eigenvalue problem in the form:

$$\mathbf{CA} = \lambda \mathbf{A}. \tag{6}$$

The eigenvector of coefficients $\mathbf{A} = \left[A(t^1), A(t^2), ..., A(t^n)\right]^T$ where $n = 1, \ldots, N$, $\mathbf{C}$ is a symmetric $N \times N$ matrix with components $C_{mn} = 1/N\left(\phi^T(\mathbf{x}, t^m)\phi(\mathbf{x}, t^n)\right)$ where $m, n = 1, 2, ..., N$ and λ is a diagonal matrix of N eigenvalues which are ordered by their variance contribution, $\lambda^1 > \lambda^2 > \lambda^3 > \cdots > \lambda^n$. Note that the eigenvalue problem defined by equation 6 needs to solved for every discretized position $\mathbf{x}$.

The solution of the eigenvalue problem results in a set of eigenfunctions, $\mathbf{A}^{(m)}$, where $m = 1, \ldots, N$. According to equation 5, the POD modes are constructed from elements of $\mathbf{A}^{(m)}$ and the original data. Normalization results in a final expression for the orthogonal basis,

$$\mathbf{\Psi}^{(m)}(\mathbf{x}) = \frac{\sum_{n=1}^{N} A^{(m)}(t^n)\boldsymbol{\phi}(\mathbf{x}, t^n)}{||\sum_{n=1}^{N} A^{(m)}(t^n)\boldsymbol{\phi}(\mathbf{x}, t^n)||}, \qquad m = 1, \ldots, N. \tag{7}$$

The instantaneous phase fraction tomograms may be reconstructed using the eigenfunctions as

$$\boldsymbol{\phi}(\mathbf{x}, t^n) = \sum_{m=1}^{N_r} a_m \mathbf{\Psi}^{(m)}(\mathbf{x}, t^n), \tag{8}$$

where the set of coefficients, a_m, are obtained by back-projecting the stochastic phase fraction tomograms onto the POD modes and N_r is the reduced number of modes. A suitable value for the latter can be obtained by inspection of the convergence rate for the sum on the right-hand side of equation 8, as will be discussed below. In the domain Ω, the coefficients are defined as

$$a_m(t^n) = \int_{\Omega} \boldsymbol{\phi}(\mathbf{x}, t^n)\mathbf{\Psi}^{(m)}(\mathbf{x}', t^n)\mathrm{d}\mathbf{x}'. \tag{9}$$

Each set of coefficients expresses the amplitude of the associated eigenmode as a function of time and the ordered basis functions allow for the largest structures of the flow to be derived from the POD. Therefore, by employing the instantaneous phase fraction as the kernel, the interface is characterized spatially via dominant structures in the critical eigenmodes. Further, the coherent structures pertaining to interfacial phase interactions are temporally illustrated by the associated set of coefficients, subcategorizing the overall flow dynamics as a function of eigenmode. In addition, the time dependent coefficients can be used in dynamical system formation (Perret *et al.*, 2006).

3. Experimental Set-up

Experiments were conducted in the Well Flow Loop of the Institute for Energy Technology (IFE). The test section is constructed of transparent PVC, with a total length of 50 m and an inner diameter of 100 mm. The ratio of length to diameter of the pipe provides sufficient development length for achieving stable slugs (Cook & Behnia, 2000). Beyond this length statistical properties of the flow structures are no longer dependent on axial position. A schematic of the test section is shown in figure 2. Enhanced mixing of the phases is produced by a static mixer operating directly after the injection site of the two fluids into the test section with flow control valves (FCV) placed intermittently along the pipe. The test section is horizontal with an accuracy of $\pm 0.1°$. Differential pressure transducers ($dP_1 - dP_7$) allowed for measurement of pressure over sections of the pipe. Broad beam gamma densitometers (G_1-G_4) produced cross-sectional averaged phase holdup while X-ray

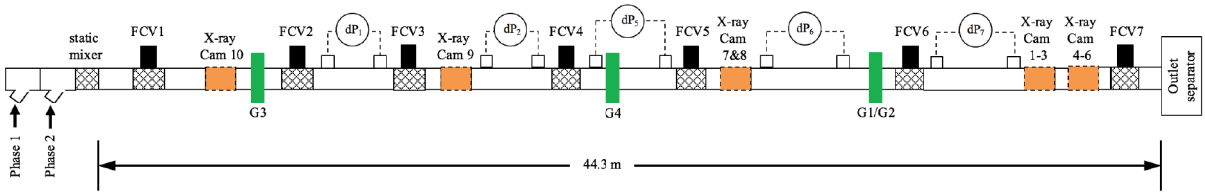

Figure 2: Experimental test section where the flow control valves are represented by FCV, the pressure transducers are denoted by dP and G_1-G_4 represent the gamma densitometers (*not to scale*).

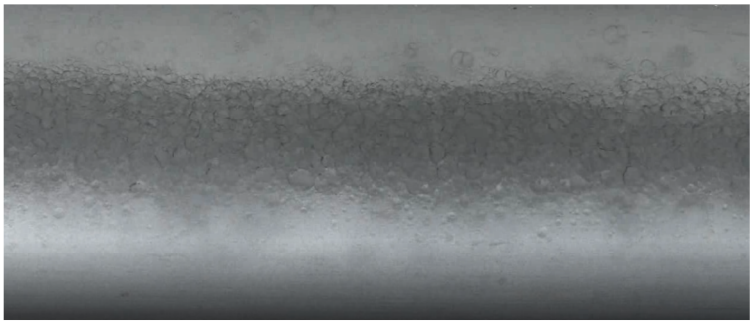

Figure 3: Still picture of dispersed flow in the Well Flow Loop during experimentation.

tomography provided local phase fraction measurements of the cross-section of the pipe. The pressure and gamma densitometer measurements are averaged over a sampling time of 15 s. **High-speed optical video as well as direct visual inspection of the PVC pipe allow the flow regime to be qualitatively visualized. Figure 3 is a still picture of the dispersed flow case and figure 4 depicts time profiles for the cross-sectional holdup of the slug flow obtained from camera 1 and camera 6.**

The X-ray computed tomography (CT) system is comprised of six point sources and six detectors, with a sampling frequency of 50 Hz. The recording time is 25 seconds, and the observed duration (time of passage in front of the camera) for the slug bodies is 1.85±0.69 seconds. A total of eleven slugs are observed during the 1250 time instances. The X-ray CT

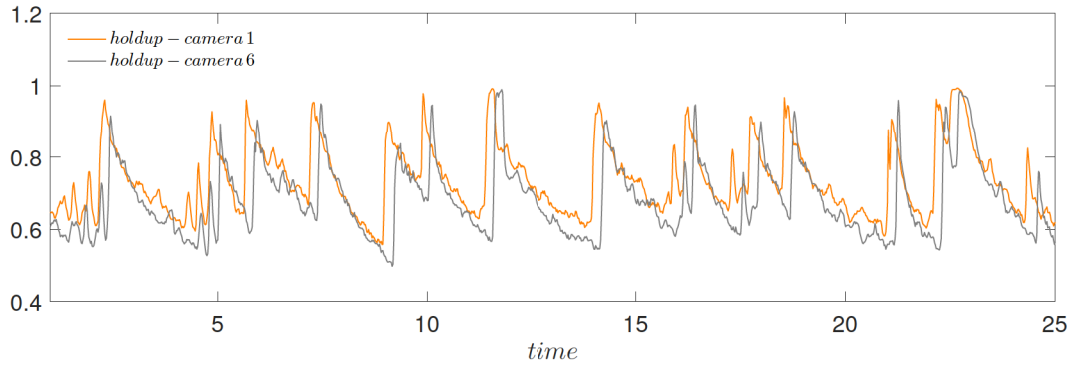

Figure 4: Time profiles for the cross-sectional oil holdup obtained via camera 1 and camera 6 for the slug flow.

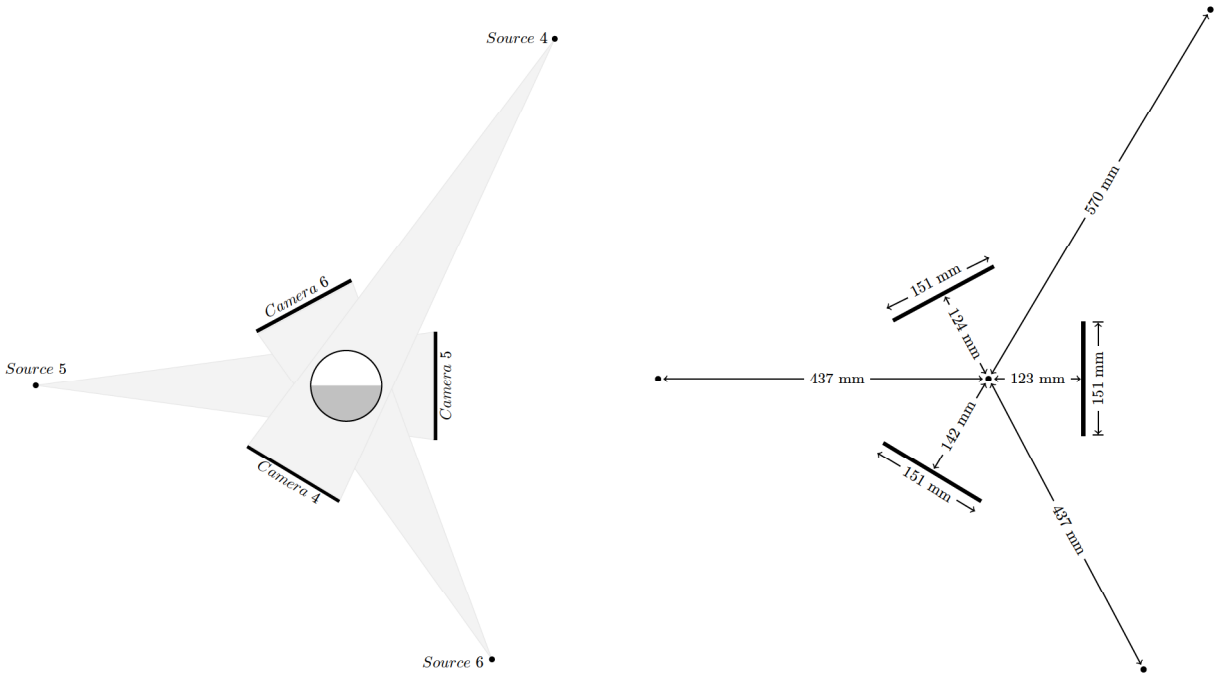

(a) (b)

Figure 5: Orientation of source and detection devices for one of the two triangular camera systems along the pipe.

system consists of two triangular setups, each containing three cameras and three sources at adjustable position along the pipe. For reference, one triangular setup is shown in figure 5. Each X-ray is attenuated as it passes through the air, the pipe wall and the fluids inside the pipe, with stronger attenuation indicated by lower intensity of camera pixel. Calibration images are obtained by filling the pipe entirely with gas, oil or water, which allow the pixel value to be converted to a holdup value for each of the phases. The resolution of a single pixel is better than 1 mm. For noise reduction, groups of neighboring pixels are averaged and the final resolution is set to a value of a few millimeters. **For the X-ray system and the materials used, the index of refraction is unity to ±0.00001, presenting insignificant contributions to the experimental results. The local uncertainty, regarding two-phase flow, for the concentration profiles obtained with each detector is a few percent. The holdup values measured by the X-ray are within ±4% uncertainty level. During tomographic construction, a certain level of statistical noise is introduced, but large and coherent features present in a given tomogram are less effected and the POD successfully locates this type of noise toward the end of the spectrum. The CT construction details are beyond the scope of this paper.**

By cross-correlating time profiles for the (cross-sectionally averaged liquid) holdup obtained at two different axial locations, the characteristic pattern velocity can be determined. In the presented experiments, X-ray images were

Regime	U_{s_g} [m/s]	U_{s_w} [m/s]	U_{s_o} [m/s]	ρ_o [kg/m^3]	ρ_w [kg/m^3]	μ_o [mPas]	μ_w [mPas]	Total snapshots
Dispersed (O-W flow)	-	0.5	0.5	803.1	996.6	1.403 ($\pm$0.02)	1.040 ($\pm$0.02)	1250
Slug (O-G flow)	0.9	-	0.6	812	-	1.42 ($\pm$0.02)	-	1250

Table 1: Experimental test conditions.

obtained at 40.27 and 40.69 meters from the inlet, respectively. The transit time between the two locations for the slugs seen in the experiment ranged from 160 ms to 280 ms, with a mean value of 242 ms. This corresponds to a characteristic pattern velocity in the range 1.50 m/s to 2.62 m/s, with a mean of $\langle U_T^{exp} \rangle = 2.06$ m/s.

In slug models in the literature, the Taylor bubble velocity is often expressed as $U_T^{theory} = C_0 \cdot U_{mix} + U_d$. The coefficient C_0 depends on the velocity distribution, and is approximately 1.05 for the presented case (Bendiksen, 1984). $U_{mix} = U_{sg} + U_{so} + U_{sw}$ is the mixture velocity, and U_d is the so-called drift velocity. For horizontal pipes, the inviscid drift velocity is given by $U_d = 0.54 \cdot \sqrt{gD} = 0.54$ m/s, where g is the gravitational acceleration, and D is the inner pipe diameter (Benjamin, 1968). For the given data, $U_T^{theory} = 1.5 + 0.54 = 2.04$ m/s. This predicted value matches reasonably well with the mean measured value U_T^{exp}, especially when one takes into account that the model assumes a single, fixed length and time scale for all slugs.

Table 1 shows details of the test parameters. The dispersed flow was comprised of Exxsol D60 oil and tap water at 20°C and a pressure of 4.1 bar. The slug flow was oil-gas flow, comprised of Exxsol D60 oil and Sulfur Hexafluoride gas (SF_6), at 20°C and a pressure of 8 bar. Each case contains 1250 time instances (snapshots). The superficial velocities for gas, water and oil are denoted as U_{s_g}, U_{s_w} and U_{s_o}, respectively.

4. Results

4.1. Time-averaged statistics

Tomograms of the mean phase fraction of oil for dispersed and slug flows are shown in figure 6. The spatial coordinates are normalized by the pipe radius, R. The mean phase fraction of oil for the dispersed flow shows a stratified layer, with a thickness of $0.25D$, located near the horizontal centerline of the pipe. There exist two symmetric pockets of $\langle \phi_o \rangle \sim 1$ in the top half of the pipe which might in part be due to imperfections in the tomographic reconstruction arising from non-exact geometry specification. An area of stratification is seen along the top edge where the phase transforms to majority water from $y/R = 0.75$ to 1. **Figure 6(b) represents the mean phase fraction of oil of the slug flow for all 1250 time instances, during which a total of eleven liquid slugs develop. To investigate the stationarity of the data, a subset of time instances for a single slug passing through the cameras was also investigated. The mean phase fraction distribution of a single slug passing compared to the entire data set of eleven liquid slugs passing showed negligible differences in its characteristics, with a maximum and mean difference of 12% and 1.7%, respectively.** Figure 6(b) shows irregular and

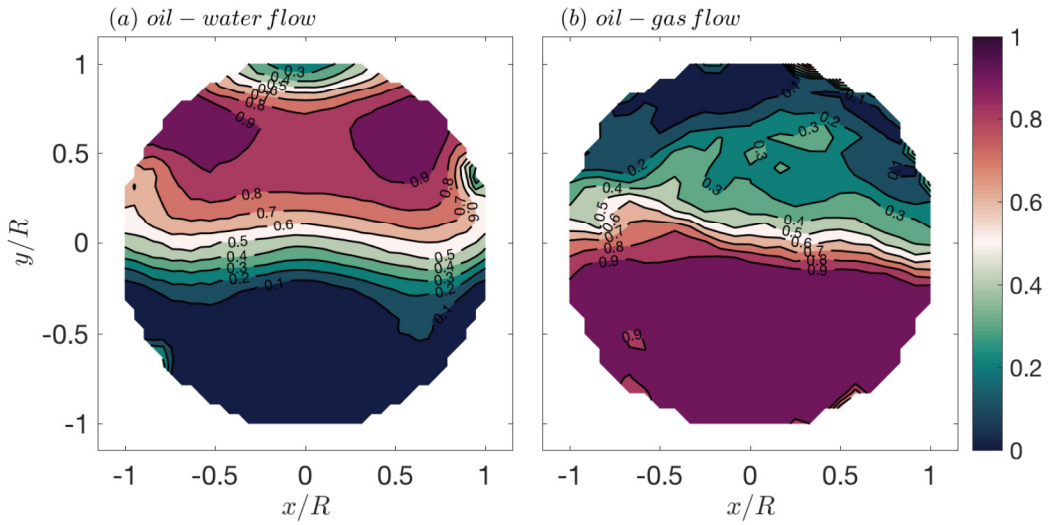

Figure 6: Mean phase fraction tomograms of the cross-sectional distribution (a) for dispersed flow and (b) for slug flow. Contour lines indicate the local oil fraction in steps of 0.1.

asymmetric stratification occurring around the horizontal centerline of the pipe. In the bottom half of the pipe, the phase fraction is almost uniformly 100% oil while the top half is a mixed flow comprised of $\langle \phi_o \rangle \sim 0$ - 0.3. **Mean slug length of the flow is computed by the experimental oil holdup detected by the vertically oriented camera (viewing the pipe from the side) and the theoretical translational velocity, U_T = 2.04 m/s, with a resulting magnitude of L_S/D = 1.53 and L/D = 37.5 The mean slug frequency, $\langle f_s \rangle$ = 0.56 (1/s).**

4.2. Proper orthogonal decomposition

Figure 7 depicts the distribution of the instantaneous phase fraction variance for the two cases as a function of the eigenvalue. The percent of variance associated with each of the first ten eigenvalues is shown, where $K_n = \lambda_n / \sum_{i=1}^{N} \lambda_i$. The percent contribution for the remaining modes is negligible. Both cases show similar trends with the first mode containing the most phase fraction variance with K_n = 99.5% and 94.0% for dispersed and slug flow, respectively. The first mode for each case shows the most dominant features of the flow field, the mean phase fraction. The first eigenmode of dispersed flow has a greater percentage of the total variance when compared with slug flow due to the regularity of the instantaneous phase fraction as a function of time. It is of note that the convergence rate is independent of the number of snapshots used for analysis.

Eigenmodes 1, 2, 3, 5, 10 and 100 obtained via POD are shown for the dispersed flow field in figure 8. The first mode, figure 8(a), represents the mean phase fraction of the flow thus, containing significant relative coherence. **Mode-2 shows a long horizontal feature that corresponds to the location of high stratification of the flow seen in figure 6.** As the mode increases, figures 8(c)-(e), features correlate to areas of fluctuation of the phase

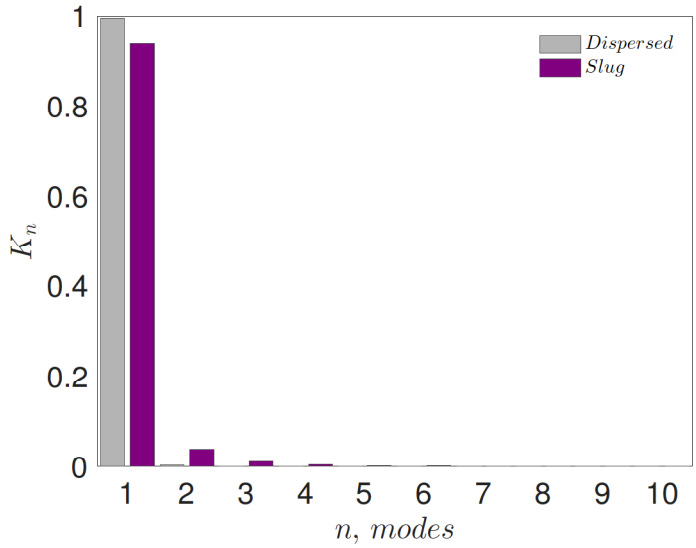

Figure 7: The distribution of variance described by normalized eigenvalues, K_n, as a function of the mode, n. Only the first ten modes are shown for clarity. The percent contribution for the remaining modes is negligible, totaling to 0.085% and 0.14% for the dispersed and slug flow respectively.

fraction and are less coherent than those seen in the first two modes. **Figure 8(c) shows three upright and nearly symmetric features while successive modes present a greater number of structures and less defined symmetry among them.** Mode 100 displays complete incoherence of the phase fraction field. **The structure present in the top of the pipe in figure 8(b) and the two small symmetric features along the pipe wall at $y/R \sim 0.5$ in mode-3 could be attributed to the small pockets of oil seen in figure 6(a). These formations may be partly due to imperfections in the tomographic construction.**

POD eigenmodes 1-3, 5, 10 and 100 for slug flow are shown in figure 9. Similar to dispersed flow, the mean phase fraction is characterized by mode-1. Eigenmodes 2, 3 and 5 show structures that correspond to the cyclical development and deployment of the liquid slug. The first and second mode reflect the basic mechanism of slug flow. The liquid slug is the region where the liquid bridges the pipe cross-section from the bottom to top and the film is the region where the flow across the pipe is separated with a pronounced interface. The gas bubble develops slowly, indicated by the bias of the structures toward the horizontal centerline of the pipe in figures 9(c) and 9(d). More specifically, the oil fills the entire pipe quickly, with oil levels moving from near centerline to the top of the pipe over one or two snapshots. The oil then gradually lowers in the pipe as the top half of the pipe fills with gas, this process takes anywhere from 0.8 to 2.6 seconds. **Mode-2 shows one main feature in the top half of the pipe while the successive modes contain flat, horizontally-oriented structures. As the eigenmode increases, the number of these structures also increases and the layered structures alternative between positive and negative magnitudes. Mode-10 follows the trend seen by modes 2, 3**

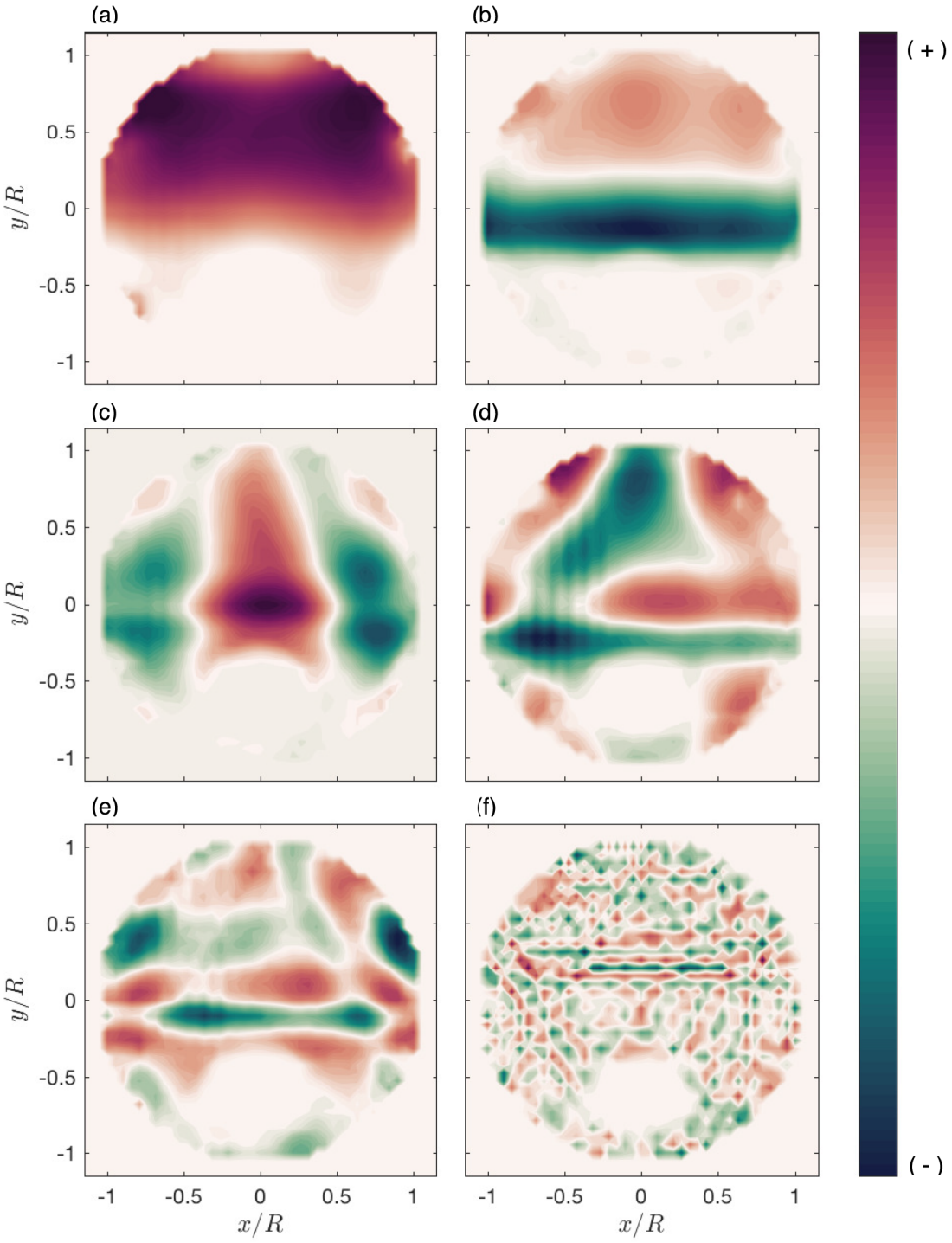

Figure 8: Eigenmodes 1, 2, 3, 5, 10 and 100 for dispersed flow are depicted in (a) through (f), respectively.

and 5 with the less pronounced features in terms of magnitude. Figure 9(f) shows complete incoherence of the flow field. **Again, there exists small features along the top of the pipe that could be attributed to measurement technique imperfections.**

The considered cases contain different features of the eigenmodes which are related to the different characteristics of the two flows. The dispersed flow is more uniform, therefore after the initial mode describing the mean phase fraction, the second mode identifies the interface between the fluids. The successive modes, figures 8(c)-(e), show structures that contain negligible significance based on their associated eigenvalue, attributed to the minimal variance that occurs during the experiment. The slug flow eigenmodes present more information about the flow field. The first two modes represent nearly 98% of the total variance present in the time series, figure 7. These modes correspond to the summation of the stratified flow and the full cross-sectional flow. The coherent features of mode-1 shows no zero-crossing across the cross-section, hence relates to the liquid slug bridging the pipe, and the coherent structure present in mode-2 represents the stratified flow within the film (or elongated bubble) region where an interface exists between the two phases. The features of the second through tenth eigenmodes correspond to the slug formation, indicating where the variation is occurring most with respect to vertical location.

Using the temporal coefficients and the eigenfunctions obtained via POD, the instantaneous phase fraction tomograms are reconstructed, as seen in equation 8. The reduced order descriptions are formed from a fixed number of POD modes, N_r, determined by the percentage of variance contribution of the ordered set of eigenvalues. The full order and reduced order descriptions of the instantaneous phase fraction tomograms of dispersed flow for a discrete set of snapshots in time are shown in figures 10(a) and (b), respectively. The full order description of the flow utilizes all 1250 degrees of freedom, therefore it includes all details of the flow field. The low order description is constructed from only the first eigenmode. Minimal differences are observed between the two figures indicating that dominant characteristics of the flow field can be described using significantly less degrees of freedom.

In figure 11, the full and reduced order descriptions of slug flow for a discrete set of snapshots containing the evolution of a slug are shown in (a) and (b), respectively. Here, the reconstructed flow field has been created using the first three modes, representing 99% of the total phase fraction variance. The magnitude of the phase fraction tomograms are slightly reduced in the low order reconstructed snapshots, but the location and overall characteristics of the slug are consistent amongst the two figures. The low order description effectively captures the interface between the phases as well as the formation and break-up of the liquid slug for the phase fraction field. This reduced order description can decrease computational time and cost during further analysis and is therefore more easily implemented into modeling programs for slug formation identification.

Phase correlation diagrams for POD modes 1, 2 and 3 for dispersed and slug flow are shown in figure 12. The dispersed flow shows minimal correlation between mode-1 and mode-2 in figure 12(a) and a negligible correlation beyond the first two modes. The trend seen between a_1 and a_2 is linear and inversely proportional signifying that as a_1 increases a_2 decreases and vice-versa. The linear trend shown between the first two modes demonstrates that the two coefficients are sufficient for recovery of the flow characteristics. The cyclical

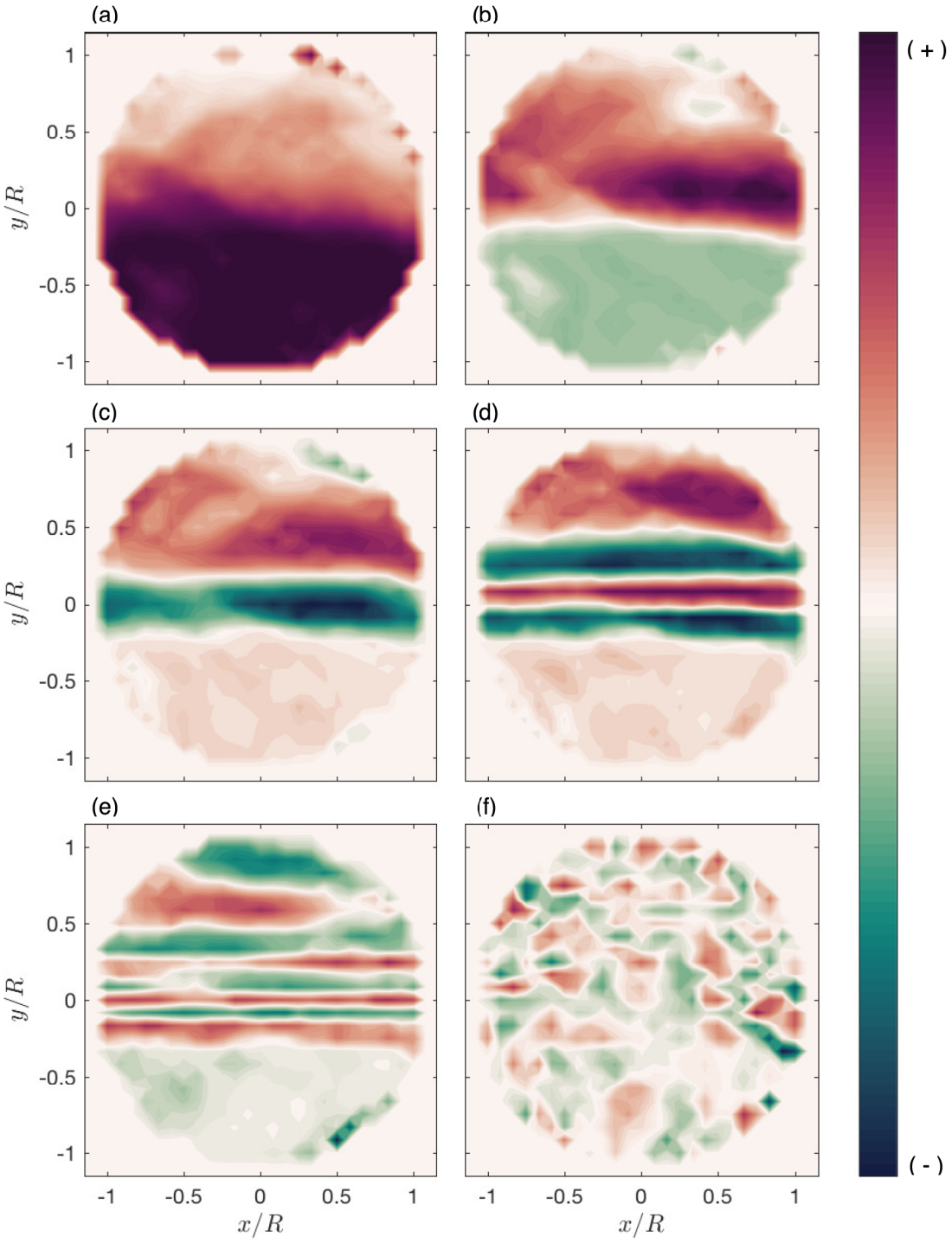

Figure 9: Eigenmodes 1, 2, 3, 5, 10 and 100 for slug flow are shown in (a) through (f), respectively.

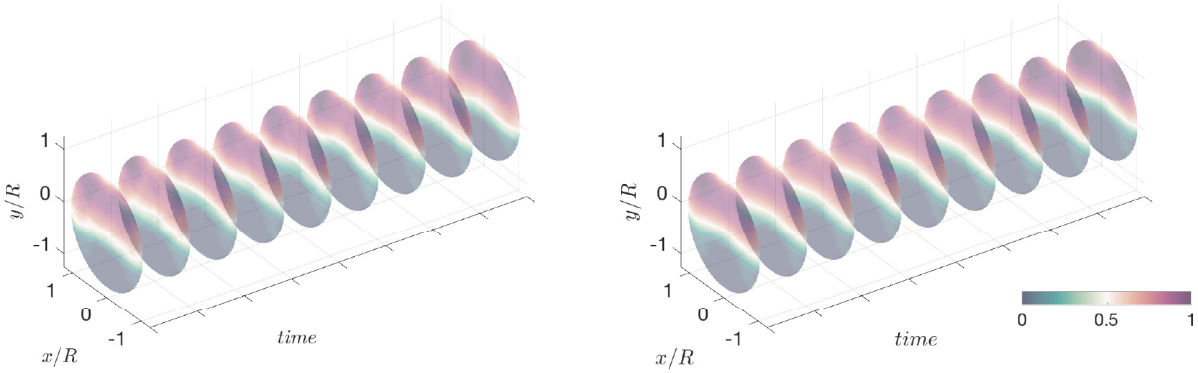

(a) (b)

Figure 10: (a) Full order instantaneous phase fraction tomograms and (b) reduced order instantaneous phase fraction tomograms of dispersed flow, reconstructed with the first eigenmode.

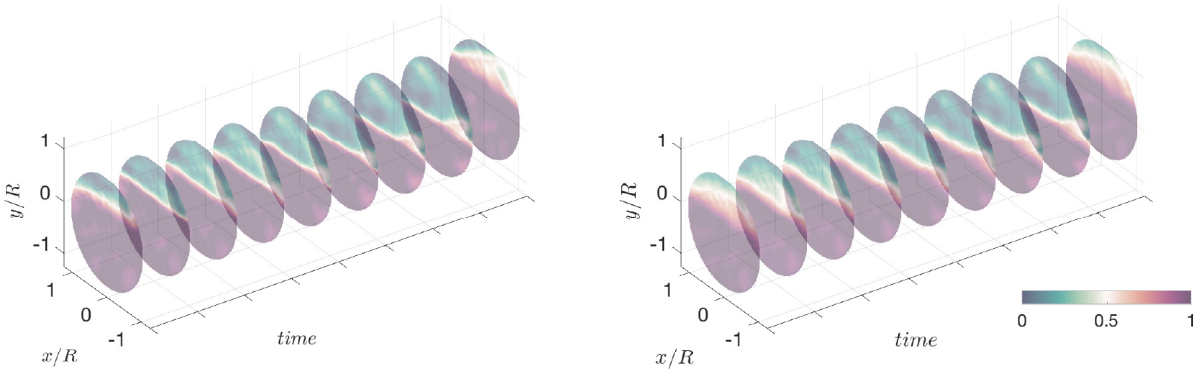

(a) (b)

Figure 11: (a) Full order instantaneous phase fraction tomograms and (b) reduced order instantaneous phase fraction tomograms of slug flow, reconstructed with the first three eigenmodes.

Coefficients	Polynomial	R^2-value
a_1 vs a_2	$0.46(a_1)^2$-$12.7a_1$+84.8	0.99
a_1 vs a_3	$0.24(a_1)^3$-$10.9(a_1)^2$+$165.1a_1$-827.1	0.92
a_2 vs a_3	$0.17(a_2)^2$-$0.45a_2$-1.9	0.93

Table 2: Phase correlation polynomial descriptions and R^2-values.

characteristics of the slug flow create correlations between the first three modes as seen in figures 12(b), 12(d) and 12(f). The development of the liquid slug spans the curves denoted in the figures by the asterisk, indicating the start of the slug and the square, signifying the end of the slug. The trends of the coefficients indicate that more than two modes are required to recover the slug. The relationship between a_1 and a_2 as well as a_2 and a_3 can be described by a second order polynomial function or curve-fit, while the curve depicted by a_1 and a_3 is best described by a third order polynomial function. Equations and corresponding R^2-values are shown in table 2. The dependence of the coefficients on liquid slug development can be correlated to other flow parameters for ease of conditional monitoring of slug passage. It is of note that describing the flow through polynomials requires high precision and errors can accumulate more quickly as the moment increases.

Two holdup profiles and the temporal coefficients, a_m, as a function of time where $m =$ 1, 2, 3 and 4 are depicted in figure 13. The included profiles, experimental and centerline holdup, refer to the holdup profile across the pipe detected by the vertically aligned camera and the holdup profile taken as a function of the vertical array located at the center of the pipe, respectively. **A value of 95% oil fraction is used as the threshold for interface identification in the pipe.** For clarity $t =$ 15-25 is omitted, the characteristics of the time steps shown are indicative of the omitted data. In figure 13(a), the experimental holdup time series displays similar trends to the centerline holdup, with fluctuations slightly emphasized. This discrepancy between the holdup profiles occurs due to the experimental holdup measurement taking the entire domain into consideration. The experimental holdup is commonly used in X-ray CT data analysis (Hu *et al.*, 2014; Schümann *et al.*, 2016) to describe the liquid holdup as a function of vertical position. This quantity directly relates to slug length based on the interface location as a function of time, equation 1. The first coefficient, although larger in magnitude, shows the same trends displayed by the two holdup profiles. The second coefficient, a_2, shows an inverse relation to the experimental and centerline holdup profiles and therefore, to the coefficient a_1. As the temporal coefficient increases, a_3, trends are muted compared to the first two coefficients, with a_4 showing negligible fluctuations. For a_2, the dispersed flow shows fluctuations limited in a small bandwidth. The magnitude of the second temporal coefficient is minimal when compared with a_1 and is directly related to the coherent structure shown in figure 8(b). The second eigenmode describes the phase fraction fluctuations in the pipe over the time series as this is second most dominant feature of the flow, insignificant in magnitude when compared with the time-averaged phase fraction, depicted by mode-1.

The oil holdup profiles in figure 13(b) exhibit cyclical fluctuations as the liquid slug develops and breaks down. Similar to the dispersed case, the experimental holdup curve

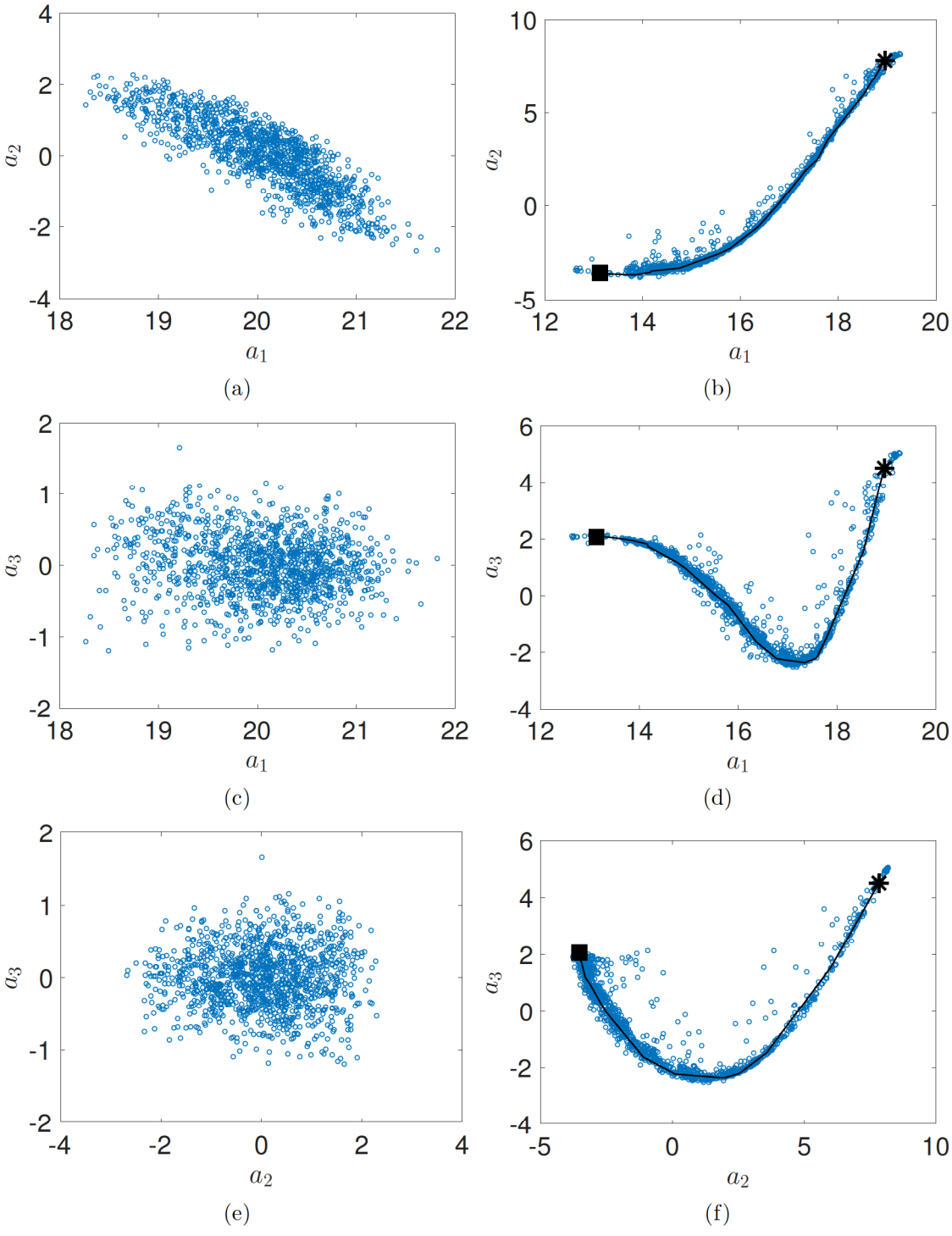

Figure 12: Phase correlation diagrams of temporal coefficients for $m = 1$, 2 and 3 for dispersed flow (left column) and slug flow (right column). The asterisk and the square, included in the figures of slug flow, represent the passage of a slug unit from $t = t_0$ to $t = t_f$, respectively.

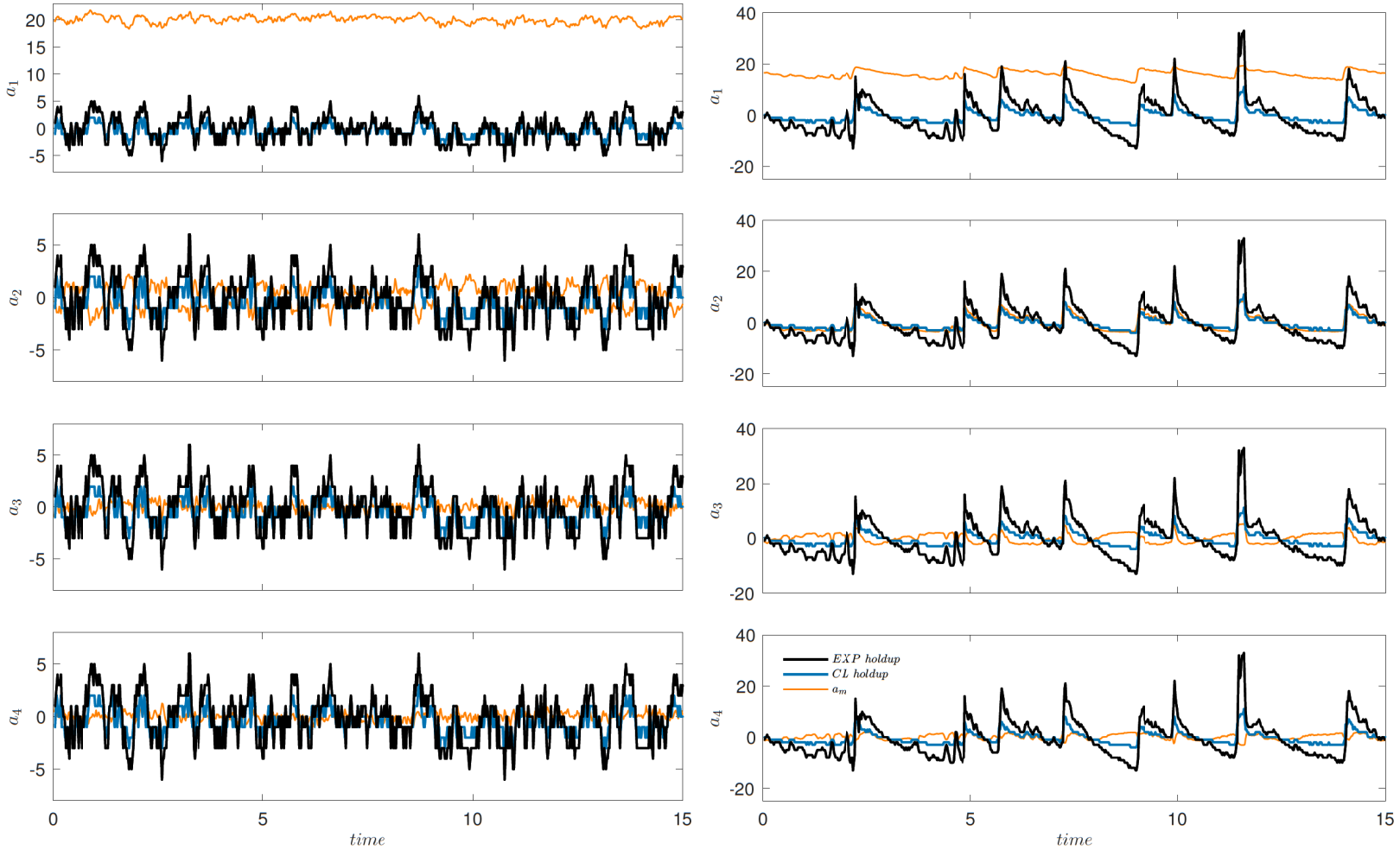

Figure 13: Experimental holdup (−), centerline holdup (−) and a_m (−) as a function of time for dispersed and slug flow in (a) and (b), respectively, where $m = 1, 2, 3$ & 4.

shows an emphasized version of the centerline holdup curve. The first coefficient displays the same tendencies revealed by the holdup profiles but with dulled features. For a_2, the centerline holdup is described well by the coefficient with the root mean squared error of 0.086,

$$RMSE = \left(\frac{1}{N} \sum_{n=1}^{N} (CL(t^n) - a_2(t^n))^2 \right)^{1/2},$$

where $CL(t^n)$ is the centerline holdup value at a given time, t^n. As the coefficient increases, $m = 3$, the coefficient shows similar characteristics to phase holdup during the first few time instances surrounding the slug formation. After the liquid slug break-up, a_3 exhibits similar fluctuations to the two holdup profiles but the temporal coefficient profile is inverted, mirroring the behavior of the two holdup curves. The fourth coefficient, a_4, shows fluctuations that are slightly muted with tendencies similar to the third coefficient. More specifically, similar to the holdup profiles during time instances surrounding the formation of the slug then quickly displaying a mirrored trend of the holdup curves after the liquid slug breaks down.

The relationship between the first coefficients and the holdup profiles is directly related to the phase correlation diagrams shown in figure 12. The inverse correlation seen in figure 12(a) is also seen in figure 13(a) by the correlation of the curves a_1 and a_2 with the holdup profiles. There is a direct correlation between a_1 and the holdup curves, and an inverse correlation between a_2 and the holdup profiles. Also, the lack of correlation between the remaining coefficients in figures 12(c) and 12(e) verify that the third coefficient does not contain prominent characteristics of the flow field.

For slug flow, the correlation between a_1 and a_2 shown in figure 12(b) is verified. The first two coefficients show similar trends with a_2 showing more emphasized representations of the holdup when compared to a_1. The third coefficient shows a direct correlation to the phase holdup profiles during liquid slug development and an inverse correlation during break-up and that can be seen by its dependence on a_1 and a_2 in figures 12(d) and (f). The third coefficient shows a direct correlation for the beginning of the slug, from the asterisks to the minimum of the curve, then a_3 is inversely related for the breaking up of the liquid slug.

The descriptions of the slug formation by the second coefficient correlate to slug length analysis in the following way: The mean slug length computed by the second temporal coefficient obtained via POD analysis, $L/D = 37.5$, is the same magnitude as the mean slug length found from the experimental holdup. Similarly, the mean slug frequency for both methods of analysis $\langle f_s \rangle = 0.56$ (1/s). The largest variation between the slug length found via experimental holdup and via POD temporal coefficients is 2.6% for this data set.

5. Conclusion

Two-phase flow loop experiments using a state-of-the-art X-ray system were investigated to further understand phase fraction characteristics for dispersed and slug flow. Proper orthogonal decomposition was performed on both cases as well as statistical analysis on

the slug flow case. The mathematical framework provided by POD describes the dominant features with reduced degrees of freedom of the systems. Descriptions of the flow dynamics via the temporal coefficients can be correlated to other flow parameters and used to develop flow control tools, improve multiphase simulations and advance predictive methodologies in numerous industrial applications.

Over the sampling time of 25 s, the dispersed flow is uniform with small fluctuations present at the liquid-liquid interface. The liquid holdup of slug flow follows a periodic profile as a function of time as liquid slugs form and break-up, with variation in frequency between the liquid slugs. The dispersed case converges to 99% of the total variance of the flow in the first mode, while slug flow reaches 99% convergence by the third mode. The eigenmodes show coherent features of the flow in only the first few modes with POD mode-1 showing the mean phase fraction of the flow for both cases. The interface of the fluids is depicted in mode-2 for dispersed flow with little coherence seen in successive modes. The interface of the slug flow exists at $0 < y/D < 1$ and is constantly in motion, which is seen by the layering of structures in modes 2, 3, 5 and 10. Reconstructions, showing dominant features of the two flow fields, are obtained with mode-1 and mode-3 for dispersed flow and slug flow, respectively. For dispersed flow, a correlation is observed between mode-1 and mode-2. Slug flow shows a high dependence between temporal coefficients for $m = 1$, 2 and 3 and a strong correlation between these coefficients and the liquid holdup. Recalling that mode-2 structures correspond to the flow of the liquid phase fully occupying the pipe, the second coefficient expresses the amplitude of the second eigenmode and therefore highlights the fluctuations at the interface. The second coefficient, a_2, describes the centerline holdup of the slug flow with high accuracy. It was observed that the mean slug length found via statistical analysis of experimental holdup values and via the second temporal coefficient, a_2, were in perfect agreement.

6. Acknowledgements

This work was in part funded by the Hydro Research Foundation.

References

Al-Safran, E., Sarica, C., Zhang, H.-Q. & Brill, J. 2005 Investigation of slug flow characteristics in the valley of a hilly-terrain pipeline. *International journal of multiphase flow* **31** (3), 337–357.

Balachandar, S. & Eaton, John K. 2010 Turbulent dispersed multiphase flow. *Annual Review of Fluid Mechanics* **42**, 111 133.

Bendiksen, K. H. 1984 An experimental investigation of the motion of long bubbles in inclined tubes. *International journal of multiphase flow* **10** (4), 467–483.

Benjamin, T. B. 1968 Gravity currents and related phenomena. *Journal of Fluid Mechanics* **31** (2), 209–248.

Brauner, N. & Ullmann, A. 2002 Modeling of phase inversion phenomenon in two-phase pipe flows. *International Journal of Multiphase Flow* **28** (7), 1177–1204.

Brenner, T. A., Fontenot, R. L., Cizmas, P. G., OBrien, T. J. & Breault, R. W. 2012 A reduced-order model for heat transfer in multiphase flow and practical aspects of the proper orthogonal decomposition. *Computers & Chemical Engineering* **43**, 68–80.

Carneiro, J. N. E., Fonseca Jr, R., Ortega, A. J., Chucuya, R. C., Nieckele, A. O. & Azevedo, L. F. A. 2011 Statistical characterization of two-phase slug flow in a horizontal pipe. *Journal of the Brazilian Society of Mechanical Sciences and Engineering* **33** (SPE1), 251–258.

Cizmas, P. G., Palacios, A., O'Brien, T. & Syamlal, M. 2003 Proper-orthogonal decomposition of spatio-temporal patterns in fluidized beds. *Chemical engineering science* **58** (19), 4417–4427.

Cook, M. & Behnia, M. 2000 Slug length prediction in near horizontal gas–liquid intermittent flow. *Chemical Engineering Science* **55** (11), 2009–2018.

Holmes, P., Lumley, J. L. & Berkooz, G. 1998 *Turbulence, coherent structures, dynamical systems and symmetry*. Cambridge University Press.

Hu, B., Langsholt, M., Liu, L., Andersson, P. & Lawrence, C. 2014 Flow structure and phase distribution in stratified and slug flows measured by x-ray tomography. *International Journal of Multiphase Flow* **67**, 162 179.

Issa, R. I. & Kempf, M. H. W. 2003 Simulation of slug flow in horizontal and nearly horizontal pipes with the two-fluid model. *International journal of multiphase flow* **29** (1), 69–95.

Kvernvold, O., Vindøy, V., Søntvedt, T., Saasen, A. & Selmer-Olsen, S. 1984 Velocity distribution in horizontal slug flow. *International journal of multiphase flow* **10** (4), 441–457.

Lindken, R. & Merzkirch, W. 2002 A novel piv technique for measurements in multiphase flows and its application to two-phase bubbly flows. *Experiments in fluids* **33** (6), 814–825.

Lumley, J. L. 1967 The structure of inhomogeneous turbulent flows. *Atmospheric turbulence and radio wave propagation* pp. 166–178.

Perret, L., Collin, E. & Delville, J. 2006 Polynomial identification of pod based low-order dynamical system. *Journal of Turbulence* (7), N17.

Schümann, H., Tutkun, M., Yang, Zhilin & Nydal, O. J. 2016 Experimental study of dispersed oil-water flow in a horizontal pipe with enhanced inlet mixing, part 1: Flow patterns, phase distributions and pressure gradients. *Journal of Petroleum Science and Engineering* **145**, 742–752.

Sirovich, L. 1987 Turbulence and the dynamics of coherent structures. Part I: Coherent structures. *Quarterly of applied mathematics* **45** (3), 561–571.

Taitel, Y. & Dukler, A. E. 1976 A model for predicting flow regime transitions in horizontal and near horizontal gas-liquid flow. *AIChE Journal* **22** (1), 47–55.

Woods, B. D., Fan, Z. & Hanratty, T. J. 2006 Frequency and development of slugs in a horizontal pipe at large liquid flows. *International Journal of Multiphase Flow* **32** (8), 902–925.